Evaluation of Transport Processes over North China Plain and Yangtze River Delta using MAX-DOAS Observations

Yuhang Song[1],#, Chengzhi Xing[2],#, Cheng Liu[1,2,3,4],*, Jinan Lin[2], Hongyu Wu[5], Ting Liu[7], Hua Lin[5], Chengxin Zhang[1], Wei Tan[2], Xiangguang Ji[5], Haoran Liu[6], and Qihua Li[6]

[1]Department of Precision Machinery and Precision Instrumentation, University of Science and Technology of China, Hefei, 230026, China

[2] Key Lab of Environmental Optics & Technology, Anhui Institute of Optics and Fine Mechanics, Hefei Institutes of Physical Science, Chinese Academy of Sciences, Hefei, 230031, China

[3]Center for Excellence in Regional Atmospheric Environment, Institute of Urban Environment, Chinese Academy of Sciences, Xiamen, 361021, China

[4]Key Laboratory of Precision Scientific Instrumentation of Anhui Higher Education Institutes, University of Science and Technology of China, Hefei, 230026, China

[5]School of Environmental Science and Optoelectronic Technology, University of Science and Technology of China, Hefei, 230026, China

[6]Institute of Physical Science and Information Technology, Anhui University, Hefei, 230601, China

[7]School of Earth and Space Sciences, University of Science and Technology of China, Hefei, 230026, China

# These two authors contributed equally to this work.
Correspondence to: Cheng Liu (chliu81@ustc.edu.cn)

Abstract. The transport of pollutants has a substantial impact on the atmospheric environment in megacity clusters. However, owing to the lack of knowledge of the vertical pollutant structure, our quantification of transport processes and understanding of their impacts on the environment remain inadequate. In this study, we retrieved the vertical profiles of aerosol, NO_2, and HCHO using multi-axis differential optical absorption spectroscopy (MAX-DOAS) and analyzed three typical transport phenomena. We found as follows: (1) The main transport layer (MTL) of aerosol, NO_2 and HCHO along the southwest–northeast transport pathway in the Jing-Jin-Ji region were approximately 400–800 m, 0–400 m and 400–1400 m, respectively. The maximum transport flux of HCHO appeared in Wangdu (WD), oppositely, the minimum transport fluxes of aerosol and NO_2 also occurred in this station. (2) The North China Plain (NCP) was usually affected by severe dust transport. The transported dust suppressed dissipation and boosted pollutant accumulation, converting the vertical profiles into an exponential shape. Furthermore, dust can indirectly affect trace gas concentrations by weakening optical intensity. For stations with higher optical intensity, the reduced NO_2 levels were closely associated with its heterogeneous reactions on dust and aerosol surfaces. Comparatively, for other stations with low solar radiation, the decreased optical intensity favored NO_2 concentration increase by inhibiting NO_2 photolysis. The reduced solar radiation favored local HCHO accumulation in Shijiazhuang (SJZ) due to the dominant contribution of primary HCHO. (3) A back-and-forth transboundary transport between the NCP and Yangtze River Delta (YRD) was found. The YRD-to-NCP and NCP-to-YRD transport processes mainly occurred in the 500–1500 m and 0–

1000 m layers, respectively. This transport, accompanied by the dome effect of aerosol, produced a large-scale $PM_{2.5}$

concentration increase, further validating the haze-amplifying mechanism by practical observations.

1 Introduction

40 With rapid economic development, urbanization in China has increased. Many cities of different scales have recently emerged, forming many megacity clusters such as Jing-Jin-Ji (JJJ) and the Yangtze River Delta (YRD). With the rapid pace of urbanization, air pollution has become one of the most serious environmental threats that China must address. Heavy air pollution adversely impacts every aspect of human life, including climate, air visibility, and human health (Pokharel et al., 2019; Gao et al., 2017; Su et al., 2020a; Li et al., 2017a).

45 Currently, air pollution sources can be roughly classified into direct emissions, secondary production, and transport. Transport remarkably contributes to pollution in some megacities. First, transportation directly deteriorates the environment through the production and emission of a large number of pollutants. Regional transport plays an important role in pollution formation in many major cities in China, such as Beijing, Shanghai, Guangzhou, Hong Kong, Hangzhou, and Chengdu, contributing more than 50% of the $PM_{2.5}$ during polluted periods (Sun et al., 2017). For the JJJ region, regional transport from southwest to

50 northeast, driven by the southwest wind, is an important factor influencing the daytime increase in $PM_{2.5}$ and O_3 concentrations (Ge et al., 2018). In addition to regional transport, cross-regional transport has important impacts. For example, intra- and inter-regional transport accounted for 25% and 28% of the total $PM_{2.5}$ in the JJJ region, respectively, from 2014 to 2017, while the local contributions was 47% (Dong et al., 2020). During the 2019 National Day parade, cross-regional dust contributed more than 74% of Beijing's particulate matter (PM) concentrations below 4 km (Wang et al., 2021). Furthermore, under certain

55 conditions, some transported pollutants can interact with the planetary boundary layer (PBL) and create an environment favorable for direct emission accumulation and secondary formation enhancement, thereby indirectly amplifying the impacts of pollution (Li et al., 2017b; Wilcox et al., 2016; Petaja et al., 2016). A typical example is the aerosols from the YRD being transported to the upper PBL over the North China Plain (NCP), which decrease the PBL heights, increasing pollutant accumulation (Huang et al., 2020). The movement of warm and humid air masses likely increases secondary aerosol formation

60 by aggravating aqueous and heterogeneous reactions (Huang et al., 2014). Hence, we must understand the air pollutant transport that occurs in megacity clusters by using an appropriate measurement method.

The current technological means of monitoring and analyzing air pollution mainly include in situ measurements, satellite observations, model simulations, and ground-based remote sensing monitoring. By 2021, the number of China National Environmental Monitoring Centers (CNEMCs), which provide in situ measurements, had extended to 2734, forming a

65 complete and mature air quality monitoring network. The CNEMCs monitor many kinds of pollutants, including SO_2, CO, NO_2, PM_{10}, $PM_{2.5}$, and O_3. However, the pollutant concentrations monitoring by the CNEMCs are limited to the ground level. Characterize pollutants in the upper-level air column using surface observations is difficult (Huang et al., 2018b) because various factors, including local emissions, regional transport, geographical factors, and meteorological conditions, need to be considered (Tao et al., 2020; Che et al., 2019). Therefore, the vertical distribution of pollutants cannot be diagnosed using only

70   the CNEMC dataset. Satellite observations can be used investigate the horizontal distribution of vertical column densities

(VCDs) of NO_2, HCHO, O_3, and aerosols on a global scale, to provide technological support for horizontal pollutant transport

analysis. However, because of their limited temporal and spatial resolutions, the data from satellites cannot be used for

continuous monitoring of a specific area. Furthermore, satellite remote sensing data cannot be used to monitor the vertical

features of and variations in the atmospheric composition (Yumimoto et al., 2016; Su et al., 2020b; Bessho et al., 2016). The

75   chemical transport model can be used to simulate pollutant distribution, and is an important tool for monitoring, forecasting,

and analyzing atmospheric quality (Huang et al., 2018a). Large uncertainties remain in pollutant distribution estimation,

primarily owing to the effects of emission inventories, meteorological fields, and hypothetical conditions (Huang et al., 2016;

Xu et al., 2016; Zhang et al., 2017). Moreover, model simulations are incapable of completely characterizing the air

composition profile because of the inadequate modeling of atmospheric pollutants in the vertical direction. To meet the need

80   for understanding the vertical distribution of air pollutants, some technical methods have been developed, such as light

detection and ranging (LiDAR) (Collis, 1966; Barrett and Ben-Dov, 1967; Wang et al., 2020) and in situ monitoring

instruments carried by aircraft, balloons, or unmanned aerial systems (UASs) (Corrigan et al., 2008; Tripathi et al., 2005;

Ferrero et al., 2011). Nevertheless, the number of detectable pollutants is limited for a single LiDAR device, and a single set

is expensive. Alternatively, monitoring based on moving platforms requires substantial labor and material resources, which

85   prevents continuous observations.

The differential optical absorption spectroscopy (DOAS) technique (Platt and Stutz, 2008) is a cutting-edge and promising

method for the quantitative analysis of many crucial atmospheric gases. DOAS uses high-frequency molecular absorption

structures in the UV and visible regions of the spectrum. Multiaxis differential optical absorption spectroscopy (MAX-DOAS),

which employs the DOAS technique at multiple elevation angles, is a tool used for long-term atmospheric quality monitoring

90   (Hönninger et al., 2004). Combined with radiative transfer modeling, MAX-DOAS can be used to retrieve the vertical profiles

of aerosols and trace gases based on scattered sunlight signals from multiple elevation angles (Frieß et al., 2006). This method

has been widely used for retrieving aerosols, HCHO, NO_2, O_3, and CHOCHO concentrations (Xing et al., 2020; Hong et al.,

2022b). Compared with the above techniques, MAX-DOAS is high resolution and low cost, and its operation is automatic.

Moreover, MAX-DOAS is capable of regularly operating in harsh environments, such as those over the Tibetan Plateau (Xing

95   et al., 2021a). On this basis, we have established nearly 30 MAX-DOAS stations covering seven regions in China (north, east,

south, northwest, southwest, northeast, and Central China) to form a mature ground-based hyperspectral stereoscopic remote

sensing network (Xing et al., 2017; Liu et al., 2021; Hong et al., 2022a). The data provided by the monitoring network

successfully meet the actual demands for vertical observations, and the network provides powerful technical support for

analyzing pollution sources and transport (Liu et al., 2022).

100 In this study, we aimed to understand the vertical distribution characteristics of air pollutants during the transport process and

analyze their possible impacts on and between regions. The remainder of this paper is structured as follows: Section 2 describes

the stations, instruments, algorithms, and ancillary data we used in the study. In Section 3, we discuss three typical transport

processes (regional, dust, and transboundary long-range transport). Finally, we present a summary and conclusions in Section

4. We think that our results will help the public gain a comprehensive understanding of the pollutant transport process and

105 provide reference values for optimization policies and regulations.

2 Method and methodology

2.1 Geographical locations and selected stations

The analyzed transport phenomena mainly occurred in the NCP and YRD, which are two of the main plain areas in China. The

NCP is partially enclosed by Mt. Taihang, Mt. Yan, and the Bohai Sea, whereas the YRD is close to the Yellow Sea and East

110 China Sea. Many megacities are located in these two regions (i.e., Beijing and Tianjin in the NCP, and Shanghai and Nanjing

in the YRD). Beijing, Tianjin, and the entire Hebei Province form large megacity clusters within the NCP, named the Beijing-

Tianjin-Hebei (BTH) region or the JJJ region. Owing to the numerous industrial factories and traffic emissions, the JJJ region

is one of the most polluted areas in China. In addition, the JJJ has a typical continental monsoon climate. The regional transport

of pollutants is prevalent within the JJJ region, which exerts serious effects on local air quality. Similarly, the YRD is affected

115 by many local pollution sources and pollutant transport. Therefore, we selected eight MAX-DOAS stations in the NCP and

YRD to explore the corresponding transport phenomena. Fig. 1 depicts the topography of the NCP and YRD and the

distribution of MAX-DOAS stations; Table S1 lists the exact latitudes and longitudes of the stations.
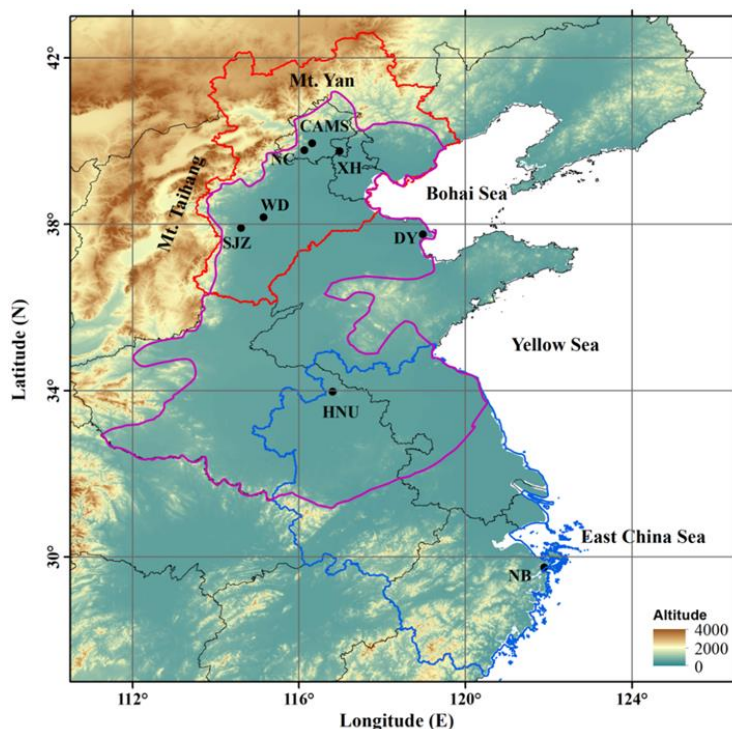
Figure 1. Study area location, topography, and distribution of MAX-DOAS stations. The black points represent the stations. The

120   **red contour: the JJJ region. The blue contour: the YRD region. The purple contour: the NCP region. The background map is**

provided by Esri 2020.

2.2 Instrument setup

We operated a commercial MAX-DOAS instrument (Airyx, Heidelberg, Germany) from January 1 to March 31, 2021, which

125   consisted of three major components: two spectrometers inside a thermoregulated box, a telescope unit, and a computer for

instrument control and data storage. One spectrometer covered the UV wavelength range (296–408 nm), and the other worked

in the visible region (420–565 nm), with a spectral resolution of 0.45 nm. The scattered sunlight was collected by a telescope

and then directed to the spectrometer through a prism reflector and quartz fiber. The instrument automatically recorded the

spectra of scattered sunlight at sequences that we set to 11 elevation angles, that is, 1°, 2°, 3°, 4°, 5°, 6°, 8°, 10°, 15°, 30°, and

130   90°. The duration of each measurement sequence was approximately 5–15 min, depending on the received radiance.

Additionally, the setup only collected scattered sunlight in the daytime, whereas the dark current and offset spectra were

automatically measured at night and removed from all the measured spectra before data analysis. To avoid the strong impact

of stratospheric absorbers, we filtered the spectra measured with a solar zenith angle (SZA) of >75°.

Table 1. Setting for the O_4, NO_2, HCHO, and HONO DOAS spectral analyses.

6

Parameter	Data source	Fitting interval			
		O_4	NO_2	HCHO	HONO
Wavelength range		338-370nm	338-370nm	322.5-358nm	335-373nm
NO_2	220 K, I_0*correction (SCD of 10^{17} molecules cm^{-2}); (Vandaele et al., 1998)	×	×	√	×
NO_2	294 K, I_0 correction (SCD of 10^{17} molecules cm^{-2}); (Vandaele et al., 1998)	√	√	√	√
O_3	223 K, I_0 correction (SCD of 10^{18} molecules cm^{-2}); (Serdyuchenko et al., 2014)	√	√	√	√
O_3	246 K, I_0 correction (SCD of 10^{18} molecules cm^{-2}); (Serdyuchenko et al., 2014)	×	×	√	×
O_4	293 K, I_0 correction (SCD of 3×10^{43} molecules cm^{-2}); (Thalman and Volkamer, 2013)	√	√	√	√
HCHO	293 K, I_0 correction (SCD of 5×10^{15} molecules cm^{-2}); (Orphal and Chance, 2003)	√	√	√	√
BrO	273 K, I_0 correction (SCD of 10^{13} molecules cm^{-2}); (Fleischmann et al., 2004)	√	√	√	√
Ring	Ring spectra calculated with DOASIS	√	√	√	√
HONO	I_0 correction (SCD of 10^{15} molecules cm^{-2}); (Stutz et al., 2000)	×	×	×	√
Polynomial degree		4	4	4	4
Intensity offset		Order 1	Order 1	Constant	Order 1

135   * Solar I_0 correction (Aliwell, 2002);

2.3 Data processing

We analyzed the spectra using DOAS Intelligent System (DOASIS) spectral fitting software, which is based on the least

squares algorithm (Kraus, 2006). First, we measured differential slant column densities (DSCDs), which is defined as the

140   difference between the off-zenith and zenith slant column densities (SCDs). Furthermore, we calculated the ring spectrum as

the measured spectrum, considering the contribution of the stratosphere to the DSCDs. We analyzed the DSCDs of the oxygen

dimer (O$_4$) and NO$_2$ in the interval between 338 and 370 nm, and we used the 322.5–358 nm and 335–373 nm wavelength

intervals for HCHO and HONO absorption analysis, respectively. We have used similar retrieval settings in our previous

studies (Xing et al., 2020; Xing et al., 2021b). Table 1 lists the detailed DOAS fitting settings for O$_4$, NO$_2$, HCHO, and HONO.

145   We included a small shift or squeeze of the wavelengths in the fitting process to compensate for the possible instability caused

by small thermal variations in the spectrograph. Fig. S1 shows a typical DOAS fit for the four species. To ensure the validity

of the retrieved data, we removed the DOAS fit results with a root mean square (RMS) larger than 1.0×10^{-3}. Moreover, to

remove the effects of clouds, we only used data with slowly varying O$_4$ DSCDs and intensities for the vertical profile retrieval.

The detailed filtering methods is provided by Chan et al. (2019). The inversion algorithm we used for aerosols and trace gases

150   is based on the optimal estimation method (OEM); we selected the radiative transfer model (RTM) library for radiative transfer

(libRadtran) as the forward model (Mayer and Kylling, 2005). We selected the cost function χ^2 to determine the maximum a

posteriori state vector x.

$$\chi^2 = (\mathbf{y} - F(\mathbf{x}, \mathbf{b}))^T \mathbf{S}_\varepsilon^{-1} (\mathbf{y} - F(\mathbf{x}, \mathbf{b})) + (\mathbf{x} - \mathbf{x}_a)^T \mathbf{S}_a^{-1} (\mathbf{x} - \mathbf{x}_a) \tag{1}$$

where $F(\boldsymbol{x}, \boldsymbol{b})$ is the forward model; $\boldsymbol{b}$ is the meteorological parameters (i.e., atmospheric pressure and temperature profiles);

155    $\boldsymbol{y}$ is the measured DSCDs; $\boldsymbol{x}_a$ is the a priori vector that serves as an additional constraint; $\boldsymbol{S}_\varepsilon$ and $\boldsymbol{S}_a$ are the covariance

matrices of $\boldsymbol{y}$ and $\boldsymbol{x}_a$, respectively. We classified the retrieval of vertical profiles of aerosols and trace gases in two steps. As

O$_4$ absorption is closely linked to the optical properties of aerosols, our first was retrieving the vertical aerosol profiles based

on the measured O$_4$ DSCDs at different elevation angles (Wittrock et al., 2003; Frieß et al., 2006; Wagner et al., 2004). In the

previous study, we proposed a new method to quickly semi-quantify the aerosol scattering and absorption properties directly

160   based on the observed UV and visible O$_4$ absorption (Xing et al., 2019). In the second step, using the retrieved aerosol

extinction profiles as the input parameter to the RTM, we obtained the NO$_2$, HCHO, and HONO vertical profiles. For this

retrieval, we separated the atmosphere into 20 layers from 0 to 3 km with a vertical resolution of 0.1 km under 1 km, and of

0.2 km from 1 to 3 km. For aerosol profile retrieval, we selected exponentially decreasing a priori with a scale height of 0.5

km. We set the a priori surface aerosol extinction to 0.2 km^{-1}. We set all the a priori uncertainties of the aerosols and trace

165   gases to 50%, and set the correlation height to 0.5 km. During the retrieval, we employed a fixed set of aerosol optical properties

with a single-scattering albedo of 0.95, an asymmetry parameter of 0.70, and a surface albedo of 0.04. A more detailed

description of the retrieval process can be found in previous studies (Chan et al., 2019; Chan et al., 2018). The profiles of

aerosols and trace gases were filtered out when the degree of freedom (DOF) was less than 1.0 and the retrieved relative error

was larger than 50% (Tan et al., 2018).

170

2.4 Error analysis

For profile retrieved results, we conduct the error analysis on the trace gas VCDs and aerosol optical density (AOD), and near-surface (0-100 m) trace gas concentrations and aerosol extinction coefficients (AECs). The error sources considered are listed below and the final results are summarized in Table 2.

175   a.   Smoothing and noise errors refers to the fitting error of DOAS fits. By calculating the averaged error of retrieved profiles, we obtained smoothing and noise errors on near-surface concentrations and column densities, which are 14 and 5 % for aerosols, 11 and 12 % for NO_2, and 14 and 15 % for HCHO.

    b.   Algorithmic error points to an imperfect minimum of the cost function, i.e., the difference between measured and modeled dSCDs. Based on the fact that measurements at 5 ° and 30 ° elevation angles are sensitive to the lower and upper air layers, respectively, the average relative differences between measured and modeled dSCDs for a 5 and 30° elevation angle are usually utilized to estimate the algorithm error on the near-surface values and column densities, respectively. Notably, algorithm error cannot be realistically estimated because it is difficult to assign the differences between measured and modelled dSCDs to each height of the profile. Considering its trivial role in the total error budget, we estimated these errors on the near-surface values and the column densities at 4 and 8 % for aerosols, 3 and 11 % for NO_2, and 4 and 11 % for HCHO, respectively, according to Wang et al. (2017).

    c.   Cross section errors are 4, 3, and 5 % for O_4 (aerosols), NO_2, and HCHO, respectively (Thalman and Volkamer, 2013; Vandaele et al., 1998; Orphal and Chance, 2003).

    d.   The errors related to the temperature dependence of the cross sections can be estimated as follows. With two cross sections at two temperatures, we firstly calculated the amplitude changes of the cross sections per kelvin. Subsequently, we multiplied this with the variation magnitude of the surrounding temperature. Due to the measurement period (from January 1 to March 31, 2021) was at the end of winter and the beginning of the spring, we conduct a rough estimation of the temperature gap as 45 K. The corresponding errors of O_4 (aerosols), NO_2, and HCHO are around 10, 2, and 6 %, respectively.

    e.   The trace gas retrieval errors associated with the effects of aerosol layers are estimated as the total error budgets of aerosol retrievals. These estimations are based on a linear propagation of the aerosol errors on the trace gas retrievals, which is a rough assumption. Given the uncertainties on aerosol properties and profiles, additional sensitivity tests should be performed for different observation geometries to derive more realistic error estimates.

The total error is calculated by combining all the error terms in Gaussian error propagation and listed in the bottom row of Table 2. We can find that smoothing and noise error plays a dominant role in the total error estimation.

200

Table 2. Averaged error estimation (in %) of the retrieved near-surface (0-100 m) trace gas concentrations and AECs, and trace gas VCDs and AOD.

	Near-surface			VCD or AOD		
	aerosol	NO$_2$	HCHO	AOD	NO$_2$	HCHO
Smoothing and noise error	14	11	14	5	12	15
Algorithm error	4	3	4	8	11	11
Cross section error	4	3	5	4	3	5
Related to temperature dependence of cross section	10	2	6	10	2	6
Related to the aerosol retrieval (only for trace gases)	-	17	17	-	14	14
Total	17	20	23	14	21	24

2.5 Transport flux calculation and main transport layer definition

205   Given the major role of pollutant transport in the JJJ region, hourly transport fluxes of each layer ($Flux_i$) and column transport fluxes ($Flux_c$) at each station were calculated to illustrate the dynamic transport process of pollutants along southwest-northeast pathway. The detailed calculation method was described below:

First, the wind speed in the southwest-northeast direction (WS) was calculated as follows:

$$WS = va \times \cos\frac{\pi}{4} + ua \times \sin\frac{\pi}{4} \tag{2}$$

210   where va and ua represented the modeling meridional wind component and zonal wind component, respectively. WS above zero meant that the wind came from the southwest and blew northeast, while WS below zero had the opposite meaning.

Then, with WS, the $Flux_i$ could be obtained:

$$Flux_i = C_i \times WS_i \tag{3}$$

Here, C_i denoted the aerosol or trace gas concentration at the altitude of the corresponding wind speed, while WS_i

215   represented the wind speed in layer i from southwest to northeast. A flux above zero indicated that the air pollutant was transported from southwest to northeast, while a flux less than zero meant that the transmission direction was from northeast to southwest.

Finally, we calculated the $Flux_c$ per unit width by summing the $Flux_i$ multiplied by the height of each layer:

$$Flux_c = \sum (Flux_i \times H_i) \tag{4}$$

220   where H_i was the height of each layer i.

For the convenience of description, the layer with high transport flux was defined as the main transport layer (MTL) for the corresponding pollutants. Equation 3 demonstrated that MTL was determined by the concentration and wind speed in the

corresponding layer. Due to the large discrepancy in their vertical distribution, the MTLs of various pollutants were bound to have different varying characteristics.

225

2.6 Ancillary data

We obtained the surface NO_2, $PM_{2.5}$, CO, and O_3 concentrations from the CNEMCs (https://quotsoft.net/air/). We simulated the wind speed and direction using Weather Research and Forecasting Model Version 4.0 (WRF 4.0). Supplement Sect. S1 details the model and parameter settings. We obtained the spatial distributions of NO_2 and HCHO from TROPOMI at a spatial

230 resolution of 3.5×7.0 km (Veefkind et al., 2012), and we obtained the spatial distributions of aerosol optical density and dust from Himawari-8 with a 0.5×2.0 km spatial resolution and a 10 min temporal resolution (Bessho et al., 2016). We calculated the 24 h backward trajectories of the air masses using the hybrid single-particle Lagrangian integrated trajectory (HYSPLIT) model (Supplement Sect. S2).

3 Results and discussion

235 For validation, we compared the surface NO_2 concentrations and aerosol extinction coefficients from MAX-DOAS measurements from January to March 2021 with in situ NO_2 and $PM_{2.5}$ collected by the CNEMCs. As displayed in Fig. 1, we found good agreement between MAX-DOAS and in situ data, with Pearson correlation coefficients (R) of 0.615 and 0.67 for aerosol and NO_2, respectively. We excluded some stations from the comparison analysis because their distance from the CNEMCs exceeded 10 km. Table S1 lists the detailed selection conditions. Furthermore, the aerosol information that we

240 directly obtained from the MAX-DOAS was the AECs. Under most conditions, aerosol mass concentration is approximately proportional to the extinction coefficient (Charlson, 1969; Robert et al., 1968). However, they were not completely equivalent; relative humidity (RH) influenced their correlation (Lv et al., 2017), which could explain the weaker aerosol correlation.
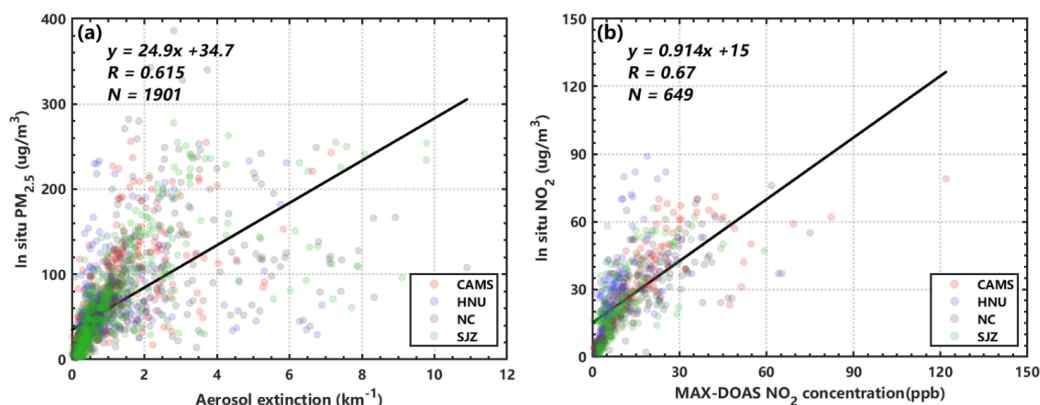
Figure 2. (a) Correlation analysis of in situ measured PM$_{2.5}$ and surface AECs (0-100 m) retrieved from CAMS, HNU, NC, and SJZ

245 **MAX-DOAS stations from January to March, 2021 and (b) their corresponding NO$_2$ comparing results. The black line denotes the**

linear least-squares fit to the data. R: Pearson correlation coefficient. N: the number of valid data.

3.1 Dynamic transport processes of NO$_2$, HCHO, and aerosol

Impacted by the semibasin topography and continental monsoon climate, intraregional transport in the JJJ region is frequent

250 and an important factor influencing the environmental air quality of many cities. Based on in situ measurements in the JJJ

region, southwest-to-northeast regional transport was found to play an important role in increasing PM$_{2.5}$ and O$_3$ levels (Ge et

al., 2018). In addition, a south-to-north transport belt exists in this region (Ge et al., 2012). Using WRF-Chem simulation, Wu

et al. (2017b) successfully evaluated the contributions of regional transport to elevated PM$_{2.5}$ and O$_3$ concentrations in Beijing

during summer. Based on vertical LiDAR observations, Xiang et al. (2021) revealed that PM$_{2.5}$ was transported to Beijing via

255 the southwest pathway. However fully understanding regional transport using model simulations or in situ measurements is

difficult. Therefore, we combined MAX-DOAS measurements with WRF simulations to more accurately describe the regional

transport processes of aerosols, NO$_2$, and HCHO. According to the TROPOMI results, we found that that NO$_2$ was

continuously distributed between SJZ and WD, whereas a HCHO distribution belt connected NC with CAMS on February 5,

2021 (Fig. S2). Fig. S3 displays the regional wind information in different layers (0–20, 200–400, 400–600, and 600–800 m),

260 with wind direction being mainly southwest–northeast among the four stations (i.e., SJZ, WD, NC, and CAMS).
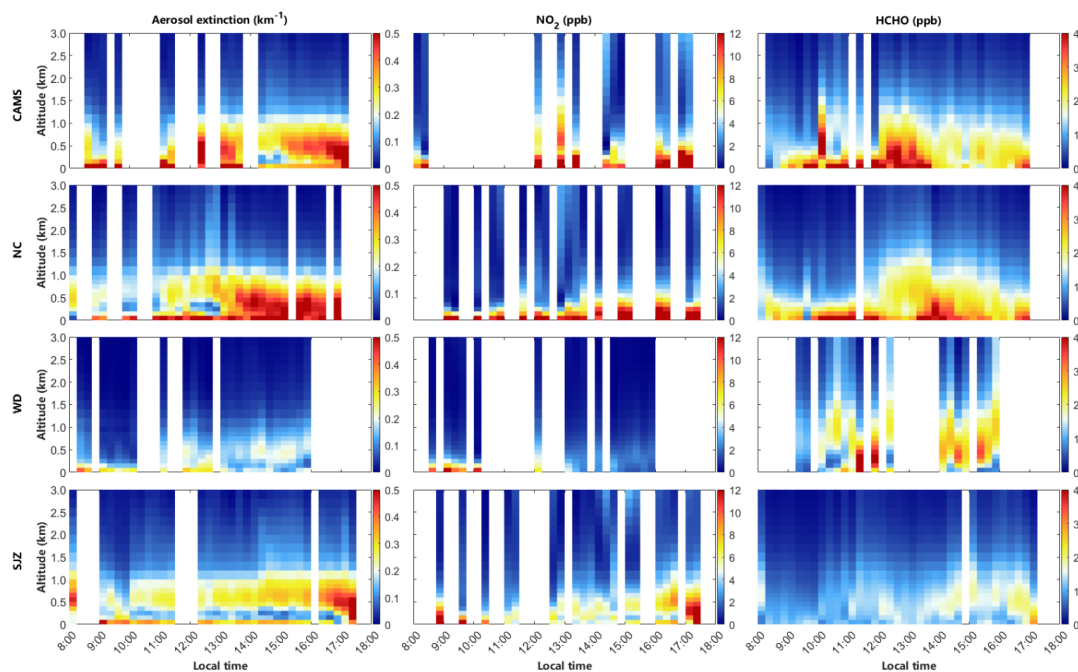
Figure 3. Vertical profiles of aerosol, NO₂, and HCHO at CAMS, NC, WD, and SJZ stations on February 5, 2021. ppb: part per billion.

265

We also identified this southwest–northeast regional transport process in the temporal variations in the vertical distributions of aerosol, NO_2, and HCHO (Fig. 3). To further demonstrate the dynamic transport process of different pollutants, we calculated the hourly $Flux_i$ and $Flux_c$, and defined the MTL. As shown in Fig. 4, the positive $Flux_i$ indicated that NO_2, HCHO, and aerosols were all transported from southwest to northeast at the four stations. The MTLs of the aerosols, HCHO,

270 and NO_2 displayed different spatiotemporal characteristics. With aerosol as an indicator, we found a high-AEC (~0.3 km^{-1}) air mass started at 400–800 m around 10:00 at SJZ (Fig. 3). Driven by the southwest wind, the aerosols were transported in the northeast direction, and we detected a relatively high AEC (~0.2 km^{-1}) over 300 m at WD around 11:00. Over time, we measured a subtle increase in AEC from ~0.2 to ~0.3 km^{-1} at 400–1000 m at NC around 12:00. Finally, we discovered an extremely high AEC (>0.5 km^{-1}) at 200–800 m at CAMS at 12:15. The MTL of aerosols mainly situated at 400–800 m during

275 the daytime and gradually dropped below 400 m in the late afternoon (Fig. 4). After 16:00, the high-extinction air mass shifted MTL from to 300–1000 m toward the surface at SJZ, with the AEC gradually exceeding 0.5 km^{-1} (Fig. 3). We observed a similar phenomenon at NC around 16:00 and at CAMS after 17:00. Surface aerosol accumulation is closely linked with the collapse of the mixing layer and the formation of a stable nocturnal boundary layer (Ding et al., 2008; Ran et al., 2016), triggering a descending tendency in the MTL. We found that a high-value NO_2 $Flux_i$ occurred in the 0–400 m layer because

13

280   NO_2 was mainly sourced from near-surface traffic emissions (Fig. 4). At the CAMS and NC stations, the NO_2 concentration was consistently high near the surface (Fig. 3), primarily because of the heavy traffic flow in Beijing. At SJZ, NO_2 concentration was high in the morning and late afternoon, whereas the concentration was lowest near noon, which we explained by the morning and evening rush hour. The variation in high-concentration NO_2 (Fig. 3) agreed well with the shift in the corresponding MTLs (Fig. 4). In addition, we determined a short-distance transport of HCHO between the NC and CAMS

285   stations. At approximately 09:30, ~2 ppb HCHO air masses first emerged in the 300–1000 m layer in the NC. Approximately half an hour later, we measured an enhanced HCHO signal (>4 ppb) at the same height at CAMS. This high-altitude transport process corroborated the HCHO regional transport belt observed by the satellite between NC and CAMS (Fig. S2b) The MTL of HCHO ranged from 400 to 1400 m, and was much more likely to extend to higher altitudes than that of aerosols or NO_2. Taking CAMS as an example, we found a strong HCHO $Flux_i$ at 600–1400 m, which lasted 4 h (10:00–14:00) (Fig. 4).

290   Likewise, the MTL of HCHO increased to over 800 m between 11:00 and 16:00 at the WD station. High HCHO concentrations tended to appear at higher altitudes than those of aerosols and NO_2 (Fig. 3). A possible explanation is that the precursor compounds of HCHO are transported to higher layers and converted into HCHO through photochemical reactions, resulting in elevated HCHO concentrations at higher altitudes (Kumar et al., 2020). Furthermore, strong high-altitude winds were more conducive to HCHO transport (Fig. S3), further increasing the corresponding transport flux (Fig. 4). Notably, HCHO $Flux_i$

295   was enhanced around noon because the increased solar radiation promoted the secondary generation of HCHO. Long-term observations revealed that secondary HCHO formation through VOC photolysis plays a large role in Beijing (Liu et al., 2020; Zhu et al., 2018). Furthermore, high concentrations of NO_2 and HCHO likely enhance the AEC at the corresponding heights (Fig. 3). Taking the CAMS results as an example, NO_2 exceeded 6 ppb at 400–800 m between 12:00 and 13:00, followed by an extreme AEC (>0.5 km^{-1}) at the same height after 12:00. At WD, high-concentration HCHO (~2.5 ppb) triggered a belt of

300   high-AEC (>0.2 km^{-1}) distribution in the 300–1200 m layer at 14:00–16:00. The increased AEC was closely linked to the generation of secondary aerosols, with HCHO and other VOCs being the main precursor compounds of organic aerosols, and NO_2 being the main precursor of inorganic aerosols. Based on the above results, we discovered that secondary aerosol generation always accompanied the regional transport process.
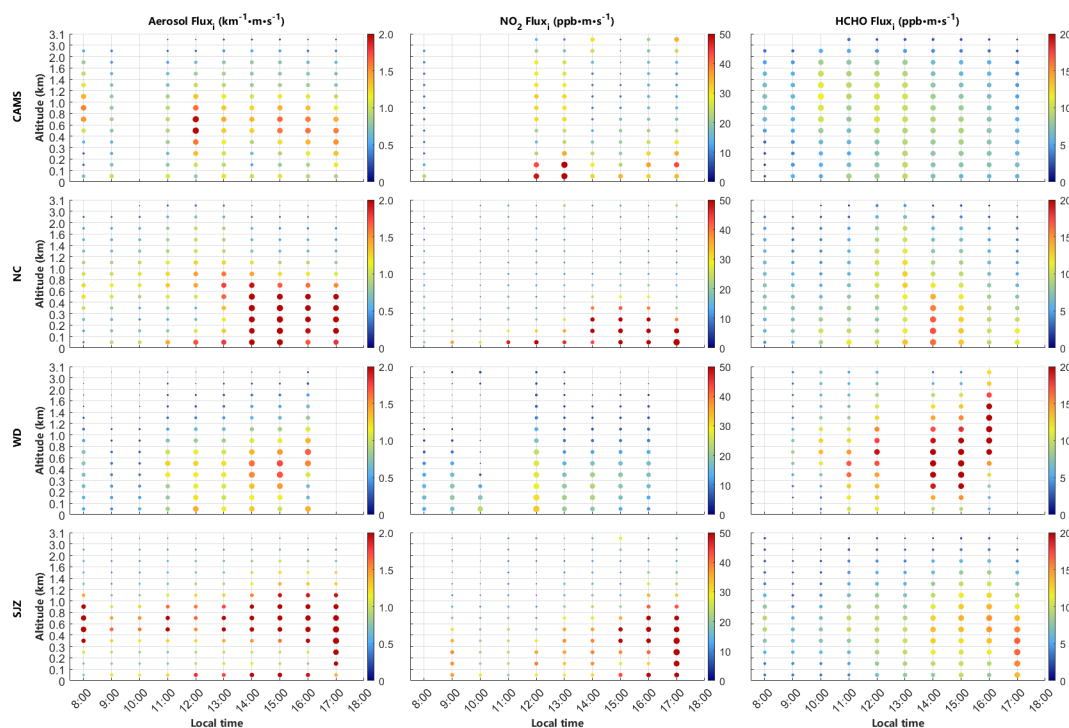
Figure 4. Transport flux per unit cross-sectional area at different altitudes ($Flux_i$) at CAMS, NC, WD, and SJZ stations on February 5, 2021.

We discovered a wide discrepancy in the $Flux_c$ among the stations for various pollutants (Fig. S4). The average aerosol $Flux_c$ decreased in the following order: SJZ (3.21×10^3 km^{-1} m^2 s^{-1}) > NC (2.69×10^3 km^{-1} m^2 s^{-1}) > CAMS (2.43×10^3 km^{-1} m^2 s^{-1}) > WD (1.42×10^3 km^{-1} m^2 s^{-1}). The largest aerosol $Flux_c$ was possibly linked to the higher wind speed at SJZ and the many surrounding pollution sources, resulting in aerosol transport. For NO$_2$ transport, the average $Flux_c$ values at SJZ (5.69×10^4 ppb m^2 s^{-1}), NC (4.42×10^4 ppb m^2 s^{-1}), and CAMS (6.16×10^4 ppb m^2 s^{-1}) were substantially higher than those at WD (2.04×10^4 ppb m^2 s^{-1}), which we attributed to higher traffic flow in Shijiazhuang and Beijing. Conversely, the average $Flux_c$ of HCHO was the highest at WD (3.21×10^4 ppb m^2 s^{-1}), whereas the $Flux_c$ values at SJZ, NC, and CAMS were 1.76×10^4, 2.01×10^4, and 1.94×10^4 ppb m^2 s^{-1}, respectively. This occurred because the WD station was located in a farm field with high vegetation coverage, so large amounts of HCHO were directly emitted by biogenic sources and secondarily produced by natural and anthropogenic VOC photolysis (Wang et al., 2016; Wu et al., 2017a). To some extent, the $Flux_c$ of various pollutants can reveal the dominant pollution species in a region. The superiority of MAX-DOAS in monitoring the vertical distribution of various pollutants was highlighted by this analysis. Combined with wind field information, we identified diverse pollutant transport processes and their corresponding MTLs, which can enable the public to gain a comprehensive understanding of pollutant transport.

15

3.2 Effects of dust transport on regional air pollution

The satellite results revealed that a dust storm had occurred in northern China on March 15, 2021 (Fig. S5), with the NCP being one of the most severely affected. Combined with the aerosol 24 h backward trajectories (Fig. S6), we found that the

325 dust storm originated in Mongolia, and its major transport pathway was Mongolia–Inner Mongolia–NCP. According to the selection standards described in Supplement Sect. S3, we confirmed that March 15 was a dusty day; we chose March 6 and 22 as comparison benchmarks because they were the nearest clean days before and after the dust storm, respectively.
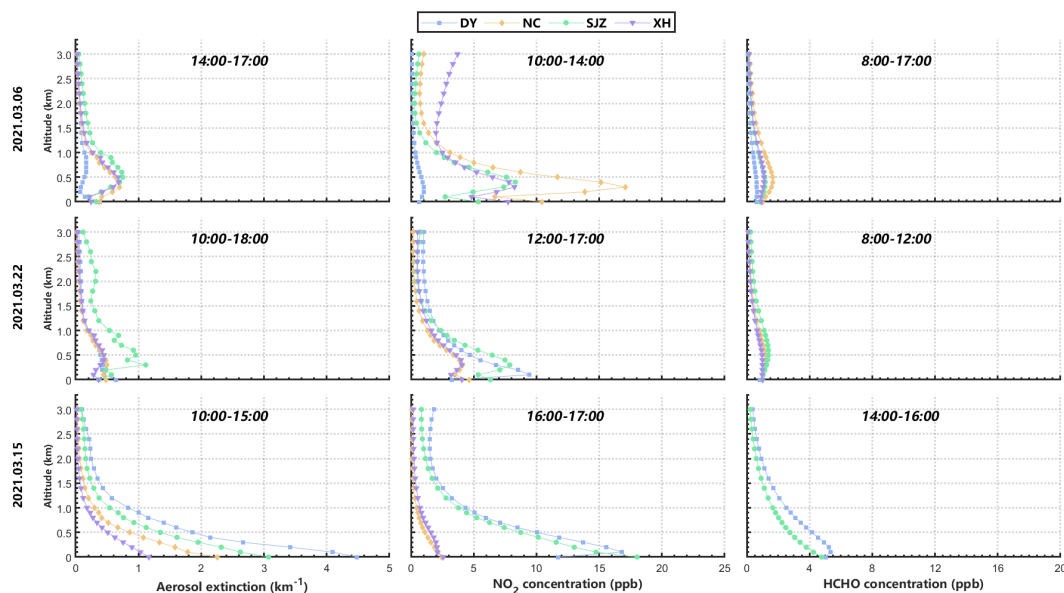
Figure 5. The daily averaged vertical profiles of AECs (left), NO₂ (middle), and HCHO (right) at DY, NC, SJZ, and XH stations
330 **during two clean days (March 6 and 22, 2021) and one dusty day (March 15, 2021). The upper annotation in each subplot represented**
their corresponding time periods, during which each station had as much data amount as possible.

The dust could suppress dissipation and aggravate local pollution accumulation. On the dust storm day, the AEC and HCHO concentrations substantially increased, especially near the surface (Fig. S7 and S9), while NO₂ concentrations also increased
335 a lot at SJZ and DY (Fig. S8). As shown in Fig. 5, we roughly classified the vertical profile shapes into multiple-peak and Gaussian shapes on clean days. For example, the AEC vertical distribution at SJZ had a two-peak shape on March 6, with a low surface peak of 0.33 km^{-1} and a high peak of 0.75 km^{-1} at 500 m (Table. S3). For the Gaussian-shaped vertical profiles, the surface concentrations remained at relatively high levels. Taking the NC results as an example, the AEC vertical distribution exhibited a Gaussian shape, with the only peak (0.70 km^{-1}) emerging at 300 m, and the surface AEC was relatively
340 high (0.38 km^{-1}). According to Liu et al. (2021), vertical profile shapes can be used to perform an overall evaluation of pollutant sources and meteorological conditions in a certain area. As discussed in Section 3.1, the prevalent regional transport strongly

16

influenced the air quality in the JJJ region, corresponding to the occurrence of high-altitude peaks. In contrast to the JJJ region, the DY station was situated in a rural area surrounded by many open oil fields and was adjacent to the Bohai Sea (Guo et al., 2010). The transport of sea salt is an important source of local aerosols (Kong et al., 2014). High-concentration surface

345   pollutants are mainly attributed to dense near-surface emission sources (e.g., traffic emissions and coal combustion). On dusty day, elevated dust concentrations weaken turbulence and decrease PBL heights, mostly through surface cooling and upper PBL heating (Mccormick and Ludwig, 1967; Li et al., 2017b; Mitchell and Jr., 1971). Unfavorable meteorological conditions not only impede pollutant dissipation and transport, but also favor the accumulation of locally produced pollutants (including direct emissions and secondary production). Therefore, during dusty periods, aerosol, NO_2, and HCHO concentrations notably

350   increased and peaked at ground level at most stations (Table. S3, S4, S5), forming an exponential profile (Fig. 5). Moreover, some accumulating components (e.g., NO_2, SO_2, and VOC) further promoted secondary aerosol formation (Huang et al., 2014). In contrast, we observed no changes in the vertical profile shapes of NO_2 and HCHO at DY. The DY station was set in a wetland with low traffic flow, and NO_2 was predominantly emitted from the surrounding higher-elevation point sources (e.g., chemical plants). Local HCHO was mainly sourced from VOC photochemical reactions that occurred at high altitudes (Chen

355   et al., 2020). Based on the above analysis, we determined why NO_2 and HCHO concentrations both peaked in the high layers, and their vertical profiles maintained a Gaussian shape. Under the influence of suppressed dissipation, the NO_2 and HCHO concentration peaks both dropped to the 100 m layer on the dusty day (Table. S4, S5). However, we found a substantial decrease in near-surface NO_2 concentrations at NC and XH on the dusty day (Fig. S6). Using the March 6 results as the benchmark, we found the near-surface NO_2 maximum concentration was 76.7% (2.43 ppb) and 66.7% lower (2.57 ppb) on

360   the dusty day at NC and XH, respectively (Fig. 5). We think that this finding is related to the critical role of heterogeneous reactions in NO_2 removal combined with optical variation; we provide detailed explanations and verifications in the paragraphs below.
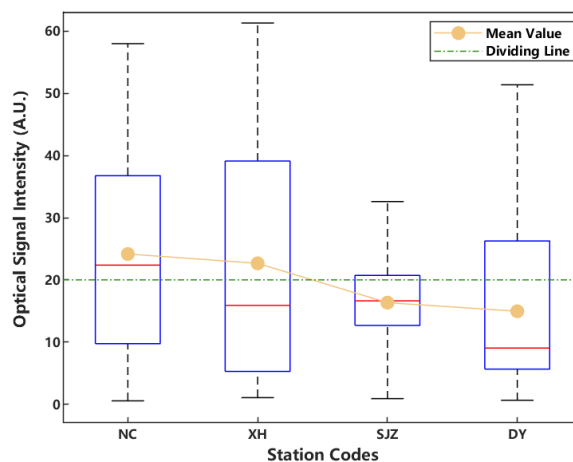
Figure 6. The daily optical intensity level at NC, XH, SJZ and DY stations on March 15, 2021. Note that the bottom and top of the

365   **box represented the 25th and 75th percentiles, respectively; the red line within the box represented the median; the yellow dot**

represented the mean; the whiskers below and above the box stood for the 10th and 90th percentiles.

In addition to aggravating pollutant accumulation, transported dust can indirectly affect regional pollution by weakening light

intensity. To determine the impact of dust on the local environment based on optical intensity variation, we classified the four

370   stations (XH, NC, SJZ, and DY) into two groups: bright group (BG) and dark group (DG), using 20 arbitrary units (A.U.) as

a threshold. In terms of optical intensity levels, we assigned NC and XH to BG, and SJZ and DY to DG (Fig. 6 and S10). For

quantification, we introduced growth rate in the comparative analysis (Supplement Section S3). For convenience, we defined

the comparison of the results of March 6 and 15, 2021, as precomparison (PRE); we defined the other between March 15 and

22, 2021 as postcomparison (POST) using March 22, 2021 as the clean day.

375   As shown in Fig. S11, the AEC noticeably increased at all stations on the dusty day, especially below 0.5 km. This occurred

not only because local accumulation was enhanced due to the decrease in PBL height, but also because the secondary

production of aerosols increased through aqueous-phase and heterogeneous chemical reactions (Ravishankara, 1997; Mcmurry

and Wilson, 1983). The AECs at DG were higher than those at BG. We mainly attributed the reduction in optical intensity to

aerosol extinction rather than dust because dust had less impact on light attenuation at 360 nm than aerosols (Wang et al.,

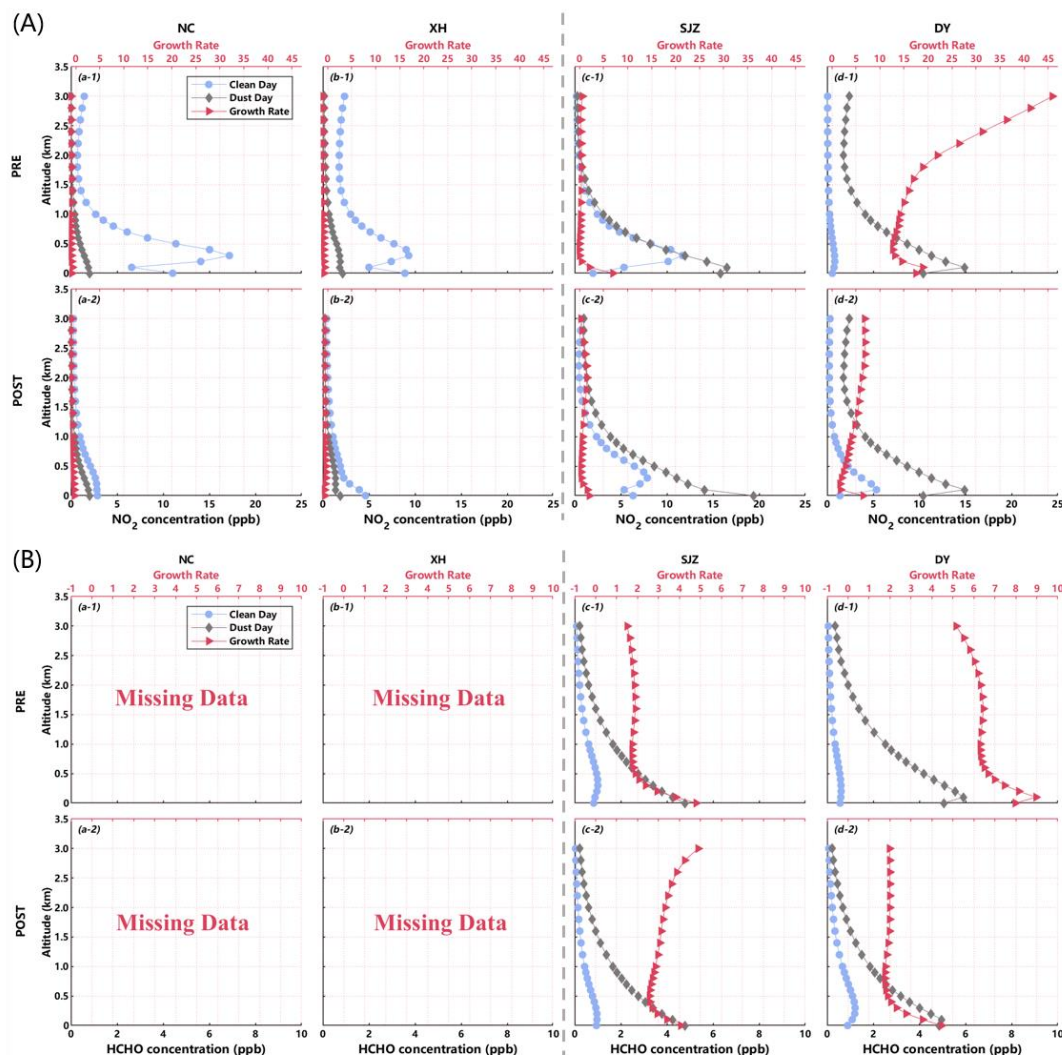380   2020). Therefore, our obtained coefficients reflected the level of aerosol extinction.

Figure 7. The growth rates of (A) NO₂ and (B) HCHO at different altitudes at (a) NC, (b) XH, (c) SJZ, and (d) DY stations. The dashed line was a dividing line. The stations on the left of the dashed line represented the bright group (BG) while two stations assigned to the dark group (DG) located on the right. PRE: precomparison results between March 6 and 15, 2021. POST: postcomparison results between March 22 and 15, 2021.

In contrast with aerosols, we observed large differences in the NO_2 growth rates between BG and DG. At DG, NO_2 concentrations exhibited a substantially increasing trend. The surface growth rates at the SJZ and DY stations were 6.97 and 17.50 in PRE, and 2.06 and 6.50 in POST, respectively (Fig. 7A (c-1, c-2, d-1, d-2)).As described above, due to the inhibited dissipation and weakened turbulent mixing caused by transported dust, surface NO_2 accumulation got intensified. Moreover, reduced solar radiation inhibits the photolysis of NO_2, which prolongs its lifetime and favors its accumulation (Chang and

Allen, 2006). In contrast, we observed decreased NO_2 concentrations at almost every height at BG. The near-surface growth

rates at NC and XH were -0.81 and -0.76 in the PRE, and -0.30 and -0.59 in the POST, respectively (Fig. 7A (a-1, a-2, b-1, b-

2)). On the dusty day, the large amounts of dust and aerosols provided surface areas for heterogeneous reactions and the

395   deposition of different trace gases. Heterogeneous reactions on dust surfaces can result in a general decrease in the atmospheric

concentrations of trace gases, such as O_3, nitrogen oxides, and hydrogen oxides (Kumar et al., 2014; Bauer, 2004; Dentener et

al., 1996). Among these reactions, the conversion of NO_x (NO + NO_2) to HONO plays an important role in NO_2 removal

(Stemmler et al., 2006; Ndour et al., 2008; George et al., 2005). Under high AEC and RH conditions, the conversion of NO_2

to HONO is further promoted (Xing et al., 2021b). With March 6 and 22 as the comparison benchmarks, we found the surface

400   growth rates in HONO concentration were 2.70 and 3.52 at NC station, respectively, which validated our speculation (Fig.

S12).

Owing to worsening meteorological conditions, increased HCHO concentrations were recorded at both the SJZ and DY

stations. In the PRE, the surface growth rate was 4.80 at SJZ (Fig. 7B (c-1)), whereas the maximum relative increase of 8.97

occurred at 100 m at DY (Fig. 7B (d-1)). In the POST, the surface concentration increasing ratio was 4.06 at SJZ, that at DY

405   was the highest (4.46) at the surface (Fig. 7B (c-2, d-2)). In addition, we noted the impact of reduced solar radiation on the

HCHO concentration. Based on the results of a linear model, we analyzed the source apportionment of ambient HCHO on

measurements from the SJZ station (Supplement Sect. S4). Primary HCHO levels played a dominant role in ambient HCHO

levels, with the total contribution ratio of primary and background HCHO exceeding 75% in March (Fig. S13b-c). The reduced

solar radiation weakened the photolysis of the primary and background HCHO, favoring the overall increase in HCHO levels

410   at SJZ. Owing to the long distance between the MAX-DOAS station and the CNEMC at DY (Table. S1), the CO and O_3

concentrations recorded by the CNEMC could not represent their corresponding concentrations around the MAX-DOAS

station. Therefore, we could not separate the source contributions of the measured HCHO concentration using the method

described above. VOCs play a dominant role in the secondary formation of HCHO at DY (Chen et al., 2022; Chen et al., 2020).

Thus, we assumed that the explosive increase in HCHO levels at DY was closely related to VOC accumulation.

415   **3.3 Spatiotemporal characteristics of aerosol during transboundary transport**

Back-and-forth transboundary long-range transport between the NCP and YRD is common, especially during winter, which

deteriorates the air quality of these two regions (Huang et al., 2020; Petaja et al., 2016). Specifically, a weak southerly wind

drives the air mass northward, causing severe pollution in the NCP (Cai et al., 2017; Callahan et al., 2019), whereas a strong

cold front increases the dissipation of the pollutants in the NCP and pushes them to the YRD (Li et al., 2018; Ding et al., 2013).

420   According to results of model simulations, the overall haze pollution is amplified during the transport process, mostly through

the mechanism of aerosol–PBL interaction (Petaja et al., 2016; Ding et al., 2016; Huang et al., 2014; Huang et al., 2018b).

Using MAX-DOAS measurements, we investigated the spatiotemporal variation in aerosols along the transport pathway and validated the haze-amplifying mechanism of this transboundary transport.

From January 18 to 20, 2021, the NCP experienced a substantial increase in aerosol concentrations, with an overall AOD
425   overpassing 0.9 (Fig. S14). Subsequently, high-concentration aerosol air masses began to move southward, gradually leaving the NCP and covering the YRD from January 21 to 22, 2021. According to the wind field and Himawari observations, a south-to-north transport belt gradually formed on January 19, 2021, which lasted nearly two days (Fig. S14 and Fig. 8). Around 12:00 on January 21, the wind direction began to change, and the north-to-south transport trend strengthened in the 0–1000 m layer on January 22 (Fig. 8 and Fig. S19). In terms of overall transport direction, we classified the MAX-DOAS monitoring
430   results into four periods: west-to-east, YRD to NCP, transformation, and NCP to YRD, to further explore their vertical characteristics during the transport process (Fig. 9).
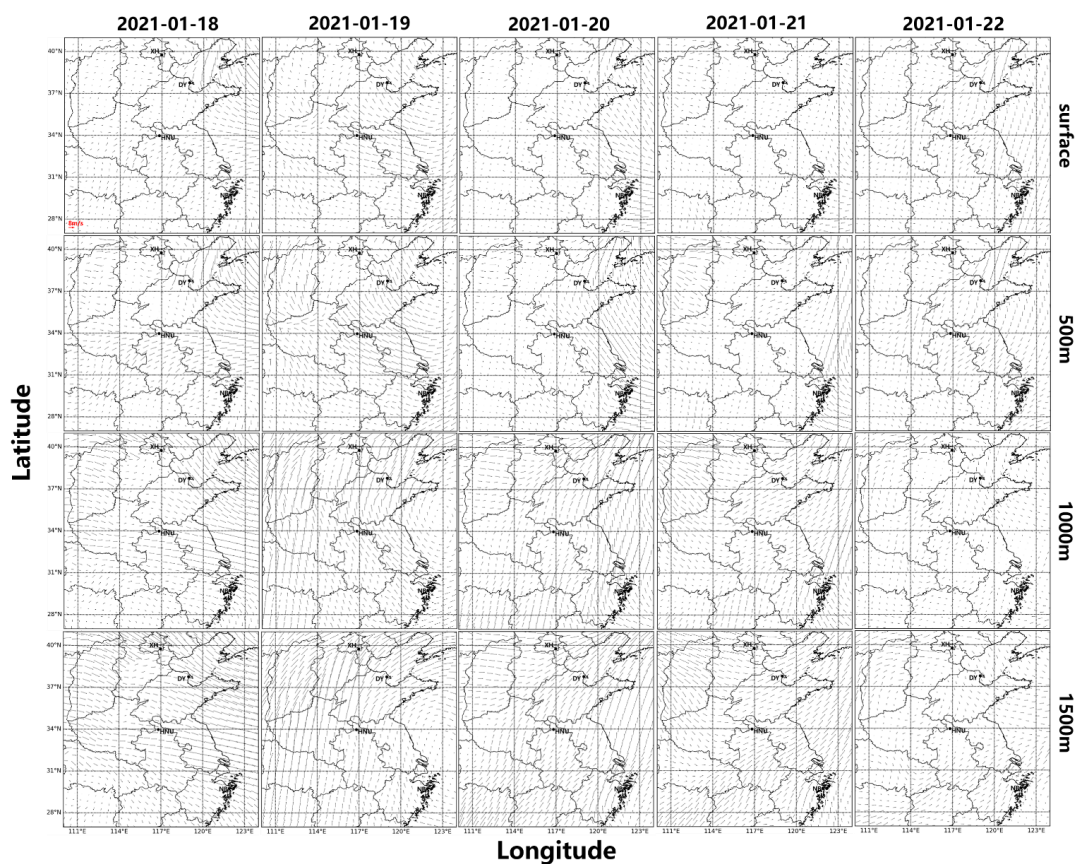

Figure 8. The wind fields in layers of surface, 500, 1000 and 1500 m at 12:00 from January 18 to 22, 2021. The red arrow in the first subgraph represents the wind speed of 8 m/s.

435

On January 18, 2021, wind gathered toward the East China Sea at every altitude, and no direct long-range transport occurred

between the NCP and YRD (Fig. S15). These two regions both had acceptable air quality, with the maximum AEC at the four

stations being less than 0.88 km^{-1} (Fig. 9) and the average PM$_{2.5}$ concentration less than 80 μg/m^3 (Fig. S20a). On January 19,

the overall AECs at all stations started to increase in varying degrees. We noted aerosol transport belts at XH in the 100–1400

440   m layer, at DY in the 200–1000 m layer, and at NB in the 100–700 m layer, with the peak AECs reaching 6.10, 1.41, and 0.96

km^{-1} at XH, DY, and NB, respectively (Fig. 9). This was closely related to the strong YRD-to-NCP transport. The results of

the wind simulation for January 19–21 indicated that the YRD-to-NCP transport mainly occurred at 500–1500 m. On January

19, the south-to-north wind direction formed in the 500–1500 m layer (Fig. S16). Meanwhile, surface transport was mainly

driven by the east wind, resulting in the PM$_{2.5}$ concentration at many western CNEMCs exceeding 80 μg/m^3 (Fig. S20b). From

445   January 20 to 21, 2021, the surface wind became so weak that near-surface transport contributed little to the local environment

(Fig. 8 and Fig. S17, S18). This also explains why the increase in near-surface AEC was less than that in the higher layers.

During this period, large amounts of aerosol from the YRD were transported to the upper layers of the NCP. In addition,

secondary particle formation intensified because the transport of warm and humid air masses favors aqueous and heterogeneous

reactions (Huang et al., 2014). These factors jointly led to a sharp increase in the AECs in the high layers at XH, DY, and NB

450   (Fig. 9). Despite the minimal contribution from surface transport, we observed a substantial increase in AEC at the ground

level on January 20–21, 2021 (Fig. 9). At DY, for example, the average surface AEC increased from 0.61 km^{-1} on January 18

to 1.03 km^{-1} on January 20, which was a 68.9% growth rate. A possible reason for this was the strong dome effect caused by

the high-layer aerosols. As a result of the aerosol–PBL interaction, PBL height decreased while temperature and humidity

increased in the lower PBL, which favored pollution accumulation and secondary aerosol production (Bharali et al., 2019;

455   Huang et al., 2020; Petaja et al., 2016). Around 12:00 on January 21, wind direction started to experience a half-day

transformation period, changing from southerly to westerly (Fig. S18). The continuous high-AEC distribution belt at NB broke

at 12:30–13:30 and 14:15–16:00 (Fig. 9), possibly owing to the western clean-air injection. The northerly wind finally formed

on January 22 and the NCP-to-YRD transport belt was created (Fig. S19). In contrast to YRD-to-NCP transport, NCP-to-YRD

transport mainly occurred at low altitudes (0–1000 m), with surface wind speeds rising to a relatively high level. Influenced

460   by strong cold fronts, large amounts of aerosols in the NCP started to disperse and gradually covered the YRD (Fig. S14),

increasing the average surface AEC at NB by 183.33% (from 1.56 to 4.42 km^{-1}) (Fig. 9). Furthermore, with 11:00 as a dividing

line, high-AEC air masses (average AEC of 0–1.6 km layer: 2.60 km^{-1}) suddenly vanished at the DY station, highlighting the

effect of quick dispersion driven by cold fronts. The weak dispersion of aerosols at XH may have been affected by anticyclones

in the JJJ region (Fig. S19). For cities in the area where the NCP and YRD overlap, their location determined that they suffered

465   a longer dome effect period because two transport processes (YRD-to-NCP and NCP-to-YRD) both passed by these areas,

producing a constant increase in pollution levels in the shallow PBL. For example, from January 18 to 22, the average AECs

in the 0–1 km layer at HNU were 0.35, 0.48, 0.75, 0.76, and 0.85 km^{-1}, respectively, showing a continuously increasing

tendency (Fig. 9). Furthermore, on January 22, extreme $PM_{2.5}$ values (>200 μg/m^3) mostly concentrated in the overlapping

zone (Fig. S20e). Generally, we found that transboundary long-range transport amplified haze pollution within the NCP and

470   YRD (Fig. 9 and Fig. S20a-e), which agrees well with previous WRF-Chem simulation results (Huang et al., 2020). This

MAX-DOAS measurements accurately demonstrated the spatiotemporal characteristics of aerosols during transboundary

transport. Furthermore, from the perspective of practical observations, we verified the haze-amplifying mechanism (Huang et

al., 2020).
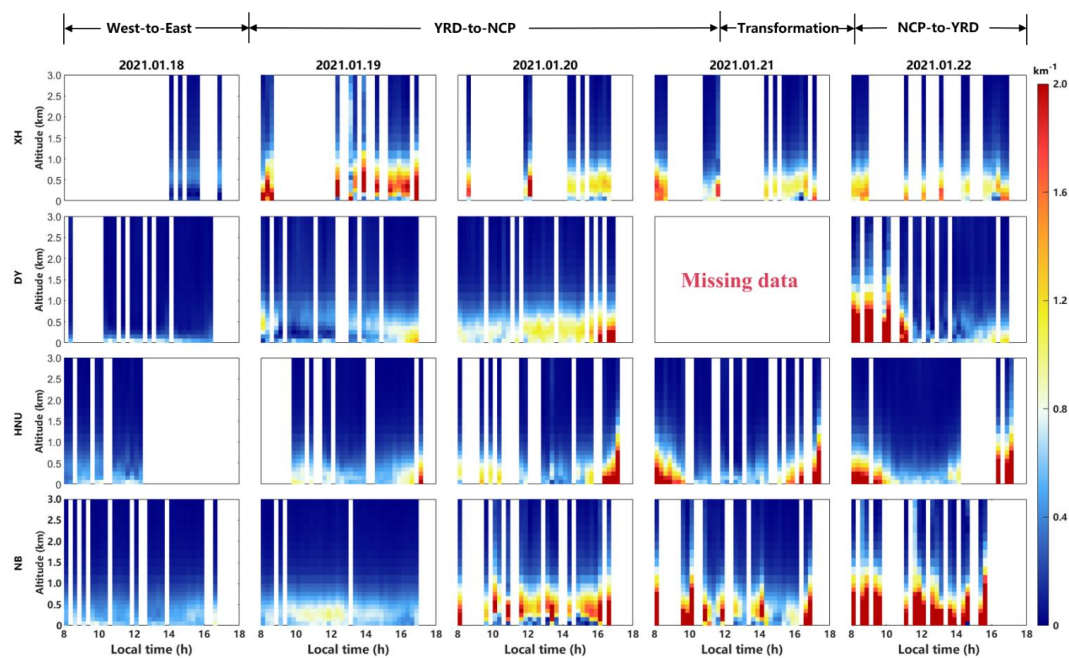
475   **Figure 9. Temporal and vertical variations in aerosol distribution at XH, DY, HNU, and NB stations from January 18 to 22, 2021.**

23

4 Conclusions

On February 5, 2021, southwest–northeast regional transport of pollutants occurred within the JJJ region. By calculating the

480      $Flux_i$ and $Flux_c$ at each selected station, we demonstrated the dynamic evolution of the MTL for aerosols, NO_2, and HCHO.

The MTL of aerosols was situated at 400–800 m during daytime, and we mainly attributed the subsequent decreasing trend

attributed to aerosol surface accumulation caused by PBL variation. Nevertheless, the MTL of NO_2 was below 400 m owing

to near-surface traffic emissions. The HCHO MTL was 400–1400 m, and extended to higher altitudes than aerosols and NO_2.

Higher HCHO concentrations and higher wind speeds at elevated altitudes jointly resulted in a higher MTL. With respect to

485   the results of $Flux_c$ comparison, we found that the outflows of aerosols and NO_2 at CAMS, NC, and SJZ were much larger

than those at WD. In contrast, the HCHO outflow at WD far exceeded the those at the other stations. This is because the WD

station was located in a farm field with high vegetation coverage, so NO_2 and aerosol emissions were lower and more HCHO

was produced from biogenic sources and VOC photolysis.

A severe dust storm occurred in the NCP along the Mongolia–Inner Mongolia–NCP pathway on March 15, 2021. On March

490   6 and 22, 2021, as clean days, dust-induced dissipation inhibition weakened pollutant transport and intensified local pollution

accumulation, eventually converting the vertical profiles into an exponential shape. The vertical profiles of NO_2 and HCHO at

DY maintained a Gaussian shape, which we explained by the elevated NO_2 emission sources and high-altitude secondary

HCHO formation. In terms of optical intensity, we classified four stations into BG and DG to examine the impact of reduced

solar radiation. High AEC growth rates occurred at all stations owing to the pollutant accumulation effect and enhanced

495   secondary formation. Moreover, the reduced optical intensity may have inhibited NO_2 photolysis, favoring NO_2 accumulation

for the DG stations. Contrarily, we observed decreases in NO_2 levels at the BG stations. The increase in HONO levels

confirmed that heterogeneous reactions on dust and aerosol surfaces played a critical role in the decreases in NO_2 levels, with

NO_x-to-HONO conversion being one of the main removal mechanisms. The results of source apportionment analysis of

ambient HCHO levels revealed that the total contributions of primary and background HCHO exceeded 75% at SJZ, with

500   primary sources playing a dominant role. The reduced solar radiation weakened the photolysis of the primary and background

HCHO levels, favoring HCHO level increases at SJZ. We mainly attributed the substantial increase in HCHO levels at DY to

VOC accumulation.

According to the results of the WRF simulation, we found that YRD-to-NCP transport mainly occurred in the upper layers

(500–1500 m). High-altitude transport triggered a substantially enhanced AEC above the NCP by directly injecting aerosols

505   and secondary particle formation. We mostly attributed the increased near-surface AEC to the dome effect produced by upper

aerosols. Subsequently, NCP-to-YRD transport, situated at 0–1000 m, dispersed the haze over the NCP and transferred low-

level aerosols to the YRD, causing a considerable increase in AEC at NB at ground level. During the entire transport process

in the zone where the NCP and YRD overlap, the AEC continuously increased in the shallow PBL owing to longer exposure

to the dome effect. Generally, this transboundary long-range transport amplified the air pollution in the two regions, verifying

510   the haze-amplifying mechanism determined based on practical observations.

In summary, accurate quantification of the vertical distribution of pollutants in air is a key requirement for understanding the

pollutant transport process. Using the MAX-DOAS network, we successfully analyzed three typical transport types (regional,

dust, and transboundary long-range transport), emphasizing the unique advantages provided by the network in monitoring

pollutant transport. We think that our findings provide the public with a thorough understanding of pollutant transport

515   phenomena and a reference for designing collaborative air pollution control strategies.

Acknowledgements

References

Aliwell, S. R.: Analysis for BrO in zenith-sky spectra: An intercomparison exercise for analysis improvement, Journal of Geophysical Research, 107, 10.1029/2001jd000329, 2002.

530   Barrett, E. W. and Ben-Dov, O.: Application of the Lidar to Air Pollution Measurements Journal of Applied Meteorology and Climatology, 6, 500-515, 10.1175/1520-0450(1967)006<0500:AOTLTA>2.0.CO;2, 1967.

Bauer, S. E.: Global modeling of heterogeneous chemistry on mineral aerosol surfaces: Influence on tropospheric ozone chemistry and comparison to observations, Journal of Geophysical Research, 109, 10.1029/2003jd003868, 2004.

Bessho, K., Date, K., Hayashi, M., Ikeda, A., Imai, T., Inoue, H., Kumagai, Y., Miyakawa, T., Murata, H., Ohno, T., Okuyama, A., Oyama,

535   R., Sasaki, Y., Shimazu, Y., Shimoji, K., Sumida, Y., Suzuki, M., Taniguchi, H., Tsuchiyama, H., Uesawa, D., Yokota, H., and Yoshida, R.: An Introduction to Himawari-8/9——Japan's New-Generation Geostationary Meteorological Satellites, Journal of the Meteorological Society of Japan. Ser. II, 94, 151-183, 10.2151/jmsj.2016-009, 2016.

Bharali, C., Nair, V. S., Chutia, L., and Babu, S. S.: Modeling of the Effects of Wintertime Aerosols on Boundary Layer Properties Over the Indo Gangetic Plain, Journal of Geophysical Research: Atmospheres, 124, 4141-4157, 10.1029/2018jd029758, 2019.

540   Cai, W., Li, K., Liao, H., Wang, H., and Wu, L.: Weather conditions conducive to Beijing severe haze more frequent under climate change, Nature Climate Change, 7, 257-262, 10.1038/nclimate3249, 2017.

Callahan, C. W., Schnell, J. L., and Horton, D. E.: Multi‐Index Attribution of Extreme Winter Air Quality in Beijing, China, Journal of Geophysical Research: Atmospheres, 124, 4567-4583, 10.1029/2018JD029738, 2019.

Chan, K. L., Wiegner, M., Wenig, M., and Pohler, D.: Observations of tropospheric aerosols and NO2 in Hong Kong over 5years using ground based MAX-DOAS, Sci Total Environ, 619-620, 1545-1556, 10.1016/j.scitotenv.2017.10.153, 2018.

Chan, K. L., Wang, Z., Ding, A., Heue, K.-P., Shen, Y., Wang, J., Zhang, F., Shi, Y., Hao, N., and Wenig, M.: MAX-DOAS measurements of tropospheric NO_2 and HCHO in Nanjing and a comparison to ozone monitoring instrument observations, Atmospheric Chemistry and Physics, 19, 10051-10071, 10.5194/acp-19-10051-2019, 2019.

Chang, S. and Allen, D. T.: Atmospheric chlorine chemistry in southeast Texas: impacts on ozone formation and control, Environmental Science & Technology, 40, 251–262, 10.1021/es050787z 2006.

Charlson, R. J.: Atmospheric visibility related to aerosol mass concentration, Environmental Science & Technology, 3, 913-918, 10.1021/es60033a002, 1969.

Che, H., Gui, K., Xia, X., Wang, Y., Holben, B. N., Goloub, P., Cuevas-Agulló, E., Wang, H., Zheng, Y., Zhao, H., and Zhang, X.: Large contribution of meteorological factors to inter-decadal changes in regional aerosol optical depth, Atmospheric Chemistry and Physics, 19, 10497-10523, 10.5194/acp-19-10497-2019, 2019.

Chen, T., Zheng, P., Zhang, Y., Dong, C., Han, G., Li, H., Yang, X., Liu, Y., Sun, J., Li, H., Zhang, X., Li, Y., Wang, W., and Xue, L.: Characteristics and formation mechanisms of atmospheric carbonyls in an oilfield region of northern China, Atmos Environ, 274, 10.1016/j.atmosenv.2022.118958, 2022.

Chen, T., Xue, L., Zheng, P., Zhang, Y., Liu, Y., Sun, J., Han, G., Li, H., Zhang, X., Li, Y., Li, H., Dong, C., Xu, F., Zhang, Q., and Wang, W.: Volatile organic compounds and ozone air pollution in an oil production region in northern China, Atmospheric Chemistry and Physics, 20, 7069-7086, 10.5194/acp-20-7069-2020, 2020.

Collis, R. T. H.: Lidar: A new atmospheric probe, Quarterly Journal of the Royal Meteorological Society, 92, 220-230, 10.1002/qj.49709239205, 1966.

Corrigan, C. E., Roberts, G. C., Ramana, M. V., Kim, D., and Ramanathan, V.: Capturing vertical profiles of aerosols and black carbon over the Indian Ocean using autonomous unmanned aerial vehicles, Atmospheric Chemistry and Physics, 8, 737–747, 10.5194/acp-8-737-2008, 2008.

Dentener, F. J., Carmichael, G. R., Zhang, Y., Lelieveld, J., and Crutzen, P. J.: Role of mineral aerosol as a reactive surface in the global troposphere, Journal of Geophysical Research: Atmospheres, 101, 22869-22889, 10.1029/96jd01818, 1996.

Ding, A. J., Wang, T., Thouret, V., Cammas, J.-P., and Nédélec, P.: Tropospheric ozone climatology over Beijing: analysis of aircraft data from the MOZAIC program, Atmospheric Chemistry and Physics, 8, 1-13, 10.5194/acp-8-1-2008, 2008.

Ding, A. J., Fu, C. B., Yang, X. Q., Sun, J. N., Zheng, L. F., Xie, Y. N., Herrmann, E., Nie, W., Petäjä, T., Kerminen, V. M., and Kulmala, M.: Ozone and fine particle in the western Yangtze River Delta: an overview of 1 yr data at the SORPES station, Atmospheric Chemistry and Physics, 13, 5813-5830, 10.5194/acp-13-5813-2013, 2013.

Ding, A. J., Huang, X., Nie, W., Sun, J. N., Kerminen, V. M., Petäjä, T., Su, H., Cheng, Y. F., Yang, X. Q., Wang, M. H., Chi, X. G., Wang, J. P., Virkkula, A., Guo, W. D., Yuan, J., Wang, S. Y., Zhang, R. J., Wu, Y. F., Song, Y., Zhu, T., Zilitinkevich, S., Kulmala, M., and Fu, C. B.: Enhanced haze pollution by black carbon in megacities in China, Geophysical Research Letters, 43, 2873-2879, 10.1002/2016gl067745, 2016.

Dong, Z., Wang, S., Xing, J., Chang, X., Ding, D., and Zheng, H.: Regional transport in Beijing-Tianjin-Hebei region and its changes during 2014-2017: The impacts of meteorology and emission reduction, Sci Total Environ, 737, 139792, 10.1016/j.scitotenv.2020.139792, 2020.

Ferrero, L., Mocnik, G., Ferrini, B. S., Perrone, M. G., Sangiorgi, G., and Bolzacchini, E.: Vertical profiles of aerosol absorption coefficient from micro-Aethalometer data and Mie calculation over Milan, Sci Total Environ, 409, 2824-2837, 10.1016/j.scitotenv.2011.04.022, 2011.

Fleischmann, O. C., Hartmann, M., Burrows, J. P., and Orphal, J.: New ultraviolet absorption cross-sections of BrO at atmospheric temperatures measured by time-windowing Fourier transform spectroscopy, J Photoch Photobio A, 168, 117-132, 10.1016/j.jphotochem.2004.03.026, 2004.

Frieß, U., Monks, P. S., Remedios, J. J., Rozanov, A., Sinreich, R., Wagner, T., and Platt, U.: MAX-DOAS O4 measurements: A new technique to derive information on atmospheric aerosols: 2. Modeling studies, Journal of Geophysical Research, 111, 10.1029/2005jd006618, 2006.

Gao, M., Saide, P. E., Xin, J., Wang, Y., Liu, Z., Wang, Y., Wang, Z., Pagowski, M., Guttikunda, S. K., and Carmichael, G. R.: Estimates of Health Impacts and Radiative Forcing in Winter Haze in Eastern China through Constraints of Surface PM2.5 Predictions, Environmental Science & Technology, 51, 2178-2185, 10.1021/acs.est.6b03745, 2017.

George, C., Strekowski, R. S., Kleffmann, J., Stemmler, K., and Ammann, M.: Photoenhanced uptake of gaseous NO2 on solid organic compounds: A photochemical source of HONO?, Faraday Discuss., 130, 195-210, 2005.

Ge, B., Wang, Z., Lin, W., Xu, X., Li, J., Ji, D., and Ma, Z.: Air pollution over the North China Plain and its implication of regional transport: A new sight from the observed evidences, Environ Pollut, 234, 29-38, 10.1016/j.envpol.2017.10.084, 2018.

Ge, B. Z., Xu, X. B., Lin, W. L., Li, J., and Wang, Z. F.: Impact of the regional transport of urban Beijing pollutants on downwind areas in summer: ozone production efficiency analysis, Tellus B: Chemical and Physical Meteorology, 64, 10.3402/tellusb.v64i0.17348, 2012.

Guo, X., He, S., Liu, K., Song, G., Wang, X., and Shi, Z.: Oil generation as the dominant overpressure mechanism in the Cenozoic Dongying depression, Bohai Bay Basin, China, AAPG Bulletin, 94, 1859-1881, 10.1306/05191009179, 2010.

Hong, Q., Liu, C., Hu, Q., Zhang, Y., Xing, C., Ou, J., Tan, W., Liu, H., Huang, X., and Wu, Z.: Vertical distribution and temporal evolution of formaldehyde and glyoxal derived from MAX-DOAS observations: The indicative role of VOC sources, Journal of Environmental Sciences, 122, 92-104, 10.1016/j.jes.2021.09.025, 2022a.

Hong, Q., Zhu, L., Xing, C., Hu, Q., Lin, H., Zhang, C., Zhao, C., Liu, T., Su, W., and Liu, C.: Inferring vertical variability and diurnal evolution of O3 formation sensitivity based on the vertical distribution of summertime HCHO and NO2 in Guangzhou, China, Sci Total Environ, 827, 154045, 10.1016/j.scitotenv.2022.154045, 2022b.

Hönninger, G., Friedeburg, C. v., and Platt, U.: Multi axis differential optical absorption spectroscopy (MAX-DOAS), Atmospheric Chemistry and Physics, 4, 231-254, 10.5194/acp-4-231-2004, 2004.

Huang, M., Crawford, J. H., Diskin, G. S., Santanello, J. A., Kumar, S. V., Pusede, S. E., Parrington, M., and Carmichael, G. R.: Modeling regional pollution transport events during KORUS-AQ: Progress and challenges in improving representation of land-atmosphere feedbacks, J Geophys Res Atmos, 123, 10732-10756, 10.1029/2018jd028554, 2018a.

Huang, R. J., Zhang, Y., Bozzetti, C., Ho, K. F., Cao, J. J., Han, Y., Daellenbach, K. R., Slowik, J. G., Platt, S. M., Canonaco, F., Zotter, P., Wolf, R., Pieber, S. M., Bruns, E. A., Crippa, M., Ciarelli, G., Piazzalunga, A., Schwikowski, M., Abbaszade, G., Schnelle-Kreis, J., Zimmermann, R., An, Z., Szidat, S., Baltensperger, U., El Haddad, I., and Prevot, A. S.: High secondary aerosol contribution to particulate pollution during haze events in China, Nature, 514, 218-222, 10.1038/nature13774, 2014.

Huang, X., Wang, Z., and Ding, A.: Impact of Aerosol‐PBL Interaction on Haze Pollution: Multiyear Observational Evidences in North China, Geophysical Research Letters, 45, 8596-8603, 10.1029/2018gl079239, 2018b.

Huang, X., Ding, A., Wang, Z., Ding, K., Gao, J., Chai, F., and Fu, C.: Amplified transboundary transport of haze by aerosol–boundary layer interaction in China, Nature Geoscience, 13, 428-434, 10.1038/s41561-020-0583-4, 2020.

Huang, X., Zhou, L., Ding, A., Qi, X., Nie, W., Wang, M., Chi, X., Petäjä, T., Kerminen, V.-M., Roldin, P., Rusanen, A., Kulmala, M., and Boy, M.: Comprehensive modelling study on observed new particle formation at the SORPES station in Nanjing, China, Atmospheric Chemistry and Physics, 16, 2477-2492, 10.5194/acp-16-2477-2016, 2016.

Kong, S., Ji, Y., Lu, B., Zhao, X., Han, B., and Bai, Z.: Similarities and Differences in PM2.5, PM10 and TSP Chemical Profiles of Fugitive Dust Sources in a Coastal Oilfield City in China, Aerosol and Air Quality Research, 14, 2017-2028, 10.4209/aaqr.2013.06.0226, 2014.

Kraus, S. G.: DOASIS: A Framework Design for DOAS, University of Mannheim, Mannheim, Germany, 2006.

Kumar, R., Barth, M. C., Madronich, S., Naja, M., Carmichael, G. R., Pfister, G. G., Knote, C., Brasseur, G. P., Ojha, N., and Sarangi, T.: Effects of dust aerosols on tropospheric chemistry during a typical pre-monsoon season dust storm in northern India, Atmospheric Chemistry and Physics, 14, 6813-6834, 10.5194/acp-14-6813-2014, 2014.

Kumar, V., Beirle, S., Dörner, S., Mishra, A. K., Donner, S., Wang, Y., Sinha, V., and Wagner, T.: Long-term MAX-DOAS measurements of NO₂, HCHO, and aerosols and evaluation of corresponding satellite data products over Mohali in the Indo-Gangetic Plain, Atmospheric Chemistry and Physics, 20, 14183-14235, 10.5194/acp-20-14183-2020, 2020.

Li, J., Du, H. Y., Wang, Z. F., Sun, Y. L., Yang, W. Y., Li, J. J., Tang, X., and Fu, P. Q.: Rapid formation of a severe regional winter haze episode over a mega-city cluster on the North China Plain, Environmental Pollution, 223, 605-615, 2017a.

Li, K., Liao, H., Cai, W., and Yang, Y.: Attribution of Anthropogenic Influence on Atmospheric Patterns Conducive to Recent Most Severe Haze Over Eastern China, Geophysical Research Letters, 45, 2072-2081, 10.1002/2017gl076570, 2018.

635   Li, Z. Q., Guo, J. P., Ding, A. J., Liao, H., Liu, J. J., Sun, Y. L., Wang, T. J., Xue, H. W., Zhang, H. S., and Zhu, B.: Aerosol and boundary-layer interactions and impact on air quality, Natl Sci Rev, 4, 810-833, 10.1093/nsr/nwx117, 2017b.

Liu, C., Xing, C., Hu, Q., Wang, S., Zhao, S., and Gao, M.: Stereoscopic hyperspectral remote sensing of the atmospheric environment: Innovation and prospects, Earth-Science Reviews, 226, 10.1016/j.earscirev.2022.103958, 2022.

Liu, C., Xing, C., Hu, Q., Li, Q., Liu, H., Hong, Q., Tan, W., Ji, X., Lin, H., Lu, C., Lin, J., Liu, H., Wei, S., Chen, J., Yang, K., Wang, S.,
640   Liu, T., and Chen, Y.: Ground-based Hyperspectral Stereoscopic Remote Sensing Network: A Promising Strategy to Learn Coordinated Control of O3 and PM2.5 over China, Engineering, 10.1016/j.eng.2021.02.019, 2021.

Liu, L., Huang, X., Ding, A., and Fu, C.: Dust-induced radiative feedbacks in north China: A dust storm episode modeling study using WRF-Chem, Atmos Environ, 129, 43-54, 10.1016/j.atmosenv.2016.01.019, 2016.

Liu, Y., Song, M., Liu, X., Zhang, Y., Hui, L., Kong, L., Zhang, Y., Zhang, C., Qu, Y., An, J., Ma, D., Tan, Q., and Feng, M.: Characterization and sources of volatile organic compounds (VOCs) and their related changes during ozone pollution days in 2016 in Beijing, China, Environ
645   Pollut, 257, 113599, 10.1016/j.envpol.2019.113599, 2020.

Lv, L., Liu, W., Zhang, T., Chen, Z., Dong, Y., Fan, G., Xiang, Y., Yao, Y., Yang, N., Chu, B., Teng, M., and Shu, X.: Observations of particle extinction, PM2.5 mass concentration profile and flux in north China based on mobile lidar technique, Atmos Environ, 164, 360-369, 10.1016/j.atmosenv.2017.06.022, 2017.

Mayer, B. and Kylling, A.: Technical note: The libRadtran software package for radiative transfer calculations – description and examples
650   of use, Atmospheric Chemistry and Physics, 5, 1855-1877, 10.5194/acp-5-1855-2005, 2005.

McCormick, R. A. and Ludwig, J. H.: Climate modification by atmospheric aerosols, Science, 156, 1358–1359, 10.1126/science.156.3780.1358, 1967.

McMurry, P. H. and Wilson, J. C.: Droplet phase (Heterogeneous) and gas phase (homogeneous) contributions to secondary ambient aerosol formation as functions of relative humidity, Journal of Geophysical Research: Oceans, 88, 5101-5108, 10.1029/JC088iC09p05101, 1983.

655   Mitchell, J. M. and Jr.: The Effect of Atmospheric Aerosols on Climate with Special Reference to Temperature near the Earth's Surface Journal of Applied Meteorology and Climatology, 10, 703–714 10.1175/1520-0450(1971)010<0703:TEOAAO>2.0.CO;2, 1971.

Ndour, M., D'Anna, B., George, C., Ka, O., Balkanski, Y., Kleffmann, J., Stemmler, K., and Ammann, M.: Photoenhanced uptake of NO2on mineral dust: Laboratory experiments and model simulations, Geophysical Research Letters, 35, 10.1029/2007gl032006, 2008.

Orphal, J. and Chance, K.: Ultraviolet and visible absorption cross-sections for HITRAN, Journal of Quantitative Spectroscopy and Radiative
660   Transfer, 82, 491-504, 10.1016/s0022-4073(03)00173-0, 2003.

Petaja, T., Jarvi, L., Kerminen, V. M., Ding, A. J., Sun, J. N., Nie, W., Kujansuu, J., Virkkula, A., Yang, X. Q., Fu, C. B., Zilitinkevich, S., and Kulmala, M.: Enhanced air pollution via aerosol-boundary layer feedback in China, Sci Rep, 6, 18998, 10.1038/srep18998, 2016.

Pokharel, M., Guang, J., Liu, B., Kang, S. C., Ma, Y. M., Holben, B. N., Xia, X. A., Xin, J. Y., Ram, K., Rupakheti, D., Wan, X., Wu, G. M., Bhattarai, H., Zhao, C. F., and Cong, Z. Y.: Aerosol Properties Over Tibetan Plateau From a Decade of AERONET Measurements:
665   Baseline, Types, and Influencing Factors, J Geophys Res-Atmos, 124, 13357-13374, 10.1029/2019jd031293, 2019.

Ran, L., Deng, Z., Xu, X., Yan, P., Lin, W., Wang, Y., Tian, P., Wang, P., Pan, W., and Lu, D.: Vertical profiles of black carbon measured by a micro-aethalometer in summer in the North China Plain, Atmospheric Chemistry and Physics, 16, 10441-10454, 10.5194/acp-16-10441-2016, 2016.

Ravishankara, A. R.: Heterogeneous and Multiphase Chemistry in the Troposphere, Science, 276, 1058-1065,
670   10.1126/science.276.5315.1058, 1997.

Robert, J. C., A., N. C., and H., H.: On the generality of correlation of atmospheric aerosol mass concentration and light scatter, Atmos Environ, 2, 455-464, 10.1016/0004-6981(68)90039-5, 1968.Serdyuchenko, A., Gorshelev, V., Weber, M., Chehade, W., and Burrows, J. P.: High spectral resolution ozone absorption cross-sections – Part 2: Temperature dependence, Atmospheric Measurement Techniques, 7, 625-636, 10.5194/amt-7-625-2014, 2014.

675   Stemmler, K., Ammann, M., Donders, C., Kleffmann, J., and George, C.: Photosensitized reduction of nitrogen dioxide on humic acid as a source of nitrous acid, Nature, 440, 195-198, 10.1038/nature04603, 2006.

Stutz, J., Kim, E. S., Platt, U., Bruno, P., Perrino, C., and Febo, A.: UV-visible absorption cross sections of nitrous acid, Journal of Geophysical Research: Atmospheres, 105, 14585-14592, 10.1029/2000jd900003, 2000.

Su, H., Cheng, Y. F., and Poschl, U.: New Multiphase Chemical Processes Influencing Atmospheric Aerosols, Air Quality, and Climate in
680   the Anthropocene, Accounts Chem Res, 53, 2034-2043, 10.1021/acs.accounts.0c00246, 2020a.

Su, W., Liu, C., Chan, K. L., Hu, Q., Liu, H., Ji, X., Zhu, Y., Liu, T., Zhang, C., Chen, Y., and Liu, J.: An improved TROPOMI tropospheric HCHO retrieval over China, Atmospheric Measurement Techniques, 13, 6271-6292, 10.5194/amt-13-6271-2020, 2020b.

Sun, J., Huang, L., Liao, H., Li, J., and Hu, J.: Impacts of Regional Transport on Particulate Matter Pollution in China: a Review of Methods and Results, Current Pollution Reports, 3, 182-191, 10.1007/s40726-017-0065-5, 2017.

685   Tan, W., Liu, C., Wang, S., Xing, C., Su, W., Zhang, C., Xia, C., Liu, H., Cai, Z., and Liu, J.: Tropospheric NO_2, SO_2, and HCHO over the East China Sea, using ship-based MAX-DOAS observations and comparison with OMI and OMPS satellite data, Atmospheric Chemistry and Physics, 18, 15387-15402, 10.5194/acp-18-15387-2018, 2018.

Tao, W., Su, H., Zheng, G., Wang, J., Wei, C., Liu, L., Ma, N., Li, M., Zhang, Q., Pöschl, U., and Cheng, Y.: Aerosol pH and chemical regimes of sulfate formation in aerosol water during winter haze in the North China Plain, Atmospheric Chemistry and Physics, 20, 11729-
690   11746, 10.5194/acp-20-11729-2020, 2020.

Thalman, R. and Volkamer, R.: Temperature dependent absorption cross-sections of O2-O2 collision pairs between 340 and 630 nm and at atmospherically relevant pressure, Phys Chem Chem Phys, 15, 15371-15381, 10.1039/c3cp50968k, 2013.

Tripathi, S. N., Dey, S., Tare, V., Satheesh, S. K., Lal, S., and Venkataramani, S.: Enhanced layer of black carbon in a north Indian industrial city, Geophysical Research Letters, 32, n/a-n/a, 10.1029/2005gl022564, 2005.

695   Vandaele, A. C., Hermans, C., Simon, P. C., Carleer, M., Colin, R., Fally, S., Merienne, M. F., Jenouvrier, A., and Coquart, B.: Measurements of the NO2 absorption cross-section from 42 000 cm(-1) to 10 000 cm(-1) (238-1000 nm) at 220 K and 294 K, Journal of Quantitative Spectroscopy & Radiative Transfer, 59, 171-184, Doi 10.1016/S0022-4073(97)00168-4, 1998.

Veefkind, J. P., Aben, I., McMullan, K., Förster, H., de Vries, J., Otter, G., Claas, J., Eskes, H. J., de Haan, J. F., Kleipool, Q., van Weele, M., Hasekamp, O., Hoogeveen, R., Landgraf, J., Snel, R., Tol, P., Ingmann, P., Voors, R., Kruizinga, B., Vink, R., Visser, H., and Levelt, P.
700   F.: TROPOMI on the ESA Sentinel-5 Precursor: A GMES mission for global observations of the atmospheric composition for climate, air quality and ozone layer applications, Remote Sensing of Environment, 120, 70-83, 10.1016/j.rse.2011.09.027, 2012.

Wagner, T., Dix, B., Friedeburg, C. v., Frieß, U., Sanghavi, S., Sinreich, R., and Platt, U.: MAX-DOAS O4 measurements: A new technique to derive information on atmospheric aerosols-Principles and information content, Journal of Geophysical Research, 109, n/a-n/a, 10.1029/2004jd004904, 2004.

705   Wang, Y., Chen, Z., Wu, Q., Liang, H., Huang, L., Li, H., Lu, K., Wu, Y., Dong, H., Zeng, L., and Zhang, Y.: Observation of atmospheric peroxides during Wangdu Campaign 2014 at a rural site in the North China Plain, Atmospheric Chemistry and Physics, 16, 10985-11000, 10.5194/acp-16-10985-2016, 2016.

Wang, Y., Lampel, J., Xie, P., Beirle, S., Li, A., Wu, D., and Wagner, T.: Ground-based MAX-DOAS observations of tropospheric aerosols, NO2, SO2 and HCHO in Wuxi, China, from 2011 to 2014, Atmospheric Chemistry and Physics, 17, 2189-2215, 10.5194/acp-17-2189-2017,
710   2017.

Wang, Z., Liu, C., Dong, Y., Hu, Q., Liu, T., Zhu, Y., and Xing, C.: Profiling of Dust and Urban Haze Mass Concentrations during the 2019 National Day Parade in Beijing by Polarization Raman Lidar, Remote Sensing, 13, 10.3390/rs13163326, 2021.

Wang, Z., Liu, C., Xie, Z., Hu, Q., Andreae, M. O., Dong, Y., Zhao, C., Liu, T., Zhu, Y., Liu, H., Xing, C., Tan, W., Ji, X., Lin, J., and Liu, J.: Elevated dust layers inhibit dissipation of heavy anthropogenic surface air pollution, Atmospheric Chemistry and Physics, 20, 14917-
715   14932, 10.5194/acp-20-14917-2020, 2020.

Wilcox, E. M., Thomas, R. M., Praveen, P. S., Pistone, K., Bender, F. A., and Ramanathan, V.: Black carbon solar absorption suppresses turbulence in the atmospheric boundary layer, Proc Natl Acad Sci U S A, 113, 11794-11799, 10.1073/pnas.1525746113, 2016.

Wittrock, F., Oetjen, H., Richter, A., Fietkau, S., Medeke, T., Rozanov, A., and Burrows, J. P.: MAX-DOAS measurements of atmospheric trace gases in Ny-Ålesund, Atmospheric Chemistry and Physics Discussions, 3, 6109-6145, hal-00301395, 2003.

720   Wu, H., Wang, Y., Li, H., Huang, L., Huang, D., Shen, H., Xing, Y., and Chen, Z.: The OH-initiated oxidation of atmospheric peroxyacetic acid: Experimental and model studies, Atmos Environ, 164, 61-70, 10.1016/j.atmosenv.2017.05.038, 2017a.

Wu, J., Li, G., Cao, J., Bei, N., Wang, Y., Feng, T., Huang, R., Liu, S., Zhang, Q., and Tie, X.: Contributions of trans-boundary transport to summertime air quality in Beijing, China, Atmospheric Chemistry and Physics, 17, 2035-2051, 10.5194/acp-17-2035-2017, 2017b.

Xia, X. and Zong, X.: Shortwave versus longwave direct radiative forcing by Taklimakan dust aerosols, Geophysical Research Letters, 36,
725   n/a-n/a, 10.1029/2009gl037237, 2009.

Xiang, Y., Zhang, T., Ma, C., Lv, L., Liu, J., Liu, W., and Cheng, Y.: Lidar vertical observation network and data assimilation reveal key processes driving the 3-D dynamic evolution of PM$_{2.5}$ concentrations over the North China Plain, Atmospheric Chemistry and Physics, 21, 7023-7037, 10.5194/acp-21-7023-2021, 2021.

Xing, C., Liu, C., Wu, H., Lin, J., Wang, F., Wang, S., and Gao, M.: Ground-based vertical profile observations of atmospheric composition on the Tibetan Plateau (2017–2019), Earth System Science Data, 13, 4897-4912, 10.5194/essd-13-4897-2021, 2021a.

Xing, C., Liu, C., Wang, S., Hu, Q., Liu, H., Tan, W., Zhang, W., Li, B., and Liu, J.: A new method to determine the aerosol optical properties from multiple-wavelength O$_4$ absorptions by MAX-DOAS observation, Atmospheric Measurement Techniques, 12, 3289-3302, 10.5194/amt-12-3289-2019, 2019.

Xing, C., Liu, C., Hu, Q., Fu, Q., Lin, H., Wang, S., Su, W., Wang, W., Javed, Z., and Liu, J.: Identifying the wintertime sources of volatile organic compounds (VOCs) from MAX-DOAS measured formaldehyde and glyoxal in Chongqing, southwest China, Sci Total Environ, 715, 136258, 10.1016/j.scitotenv.2019.136258, 2020.

Xing, C., Liu, C., Hu, Q., Fu, Q., Wang, S., Lin, H., Zhu, Y., Wang, S., Wang, W., Javed, Z., Ji, X., and Liu, J.: Vertical distributions of wintertime atmospheric nitrogenous compounds and the corresponding OH radicals production in Leshan, southwest China, J Environ Sci (China), 105, 44-55, 10.1016/j.jes.2020.11.019, 2021b.

Xing, C., Liu, C., Wang, S., Chan, K. L., Gao, Y., Huang, X., Su, W., Zhang, C., Dong, Y., Fan, G., Zhang, T., Chen, Z., Hu, Q., Su, H., Xie, Z., and Liu, J.: Observations of the vertical distributions of summertime atmospheric pollutants and the corresponding ozone production in Shanghai, China, Atmospheric Chemistry and Physics, 17, 14275-14289, 10.5194/acp-17-14275-2017, 2017.

Xu, J., Chang, L., Qu, Y., Yan, F., Wang, F., and Fu, Q.: The meteorological modulation on PM2.5 interannual oscillation during 2013 to 2015 in Shanghai, China, Sci Total Environ, 572, 1138-1149, 10.1016/j.scitotenv.2016.08.024, 2016.

Yumimoto, K., Nagao, T. M., Kikuchi, M., Sekiyama, T. T., Murakami, H., Tanaka, T. Y., Ogi, A., Irie, H., Khatri, P., Okumura, H., Arai, K., Morino, I., Uchino, O., and Maki, T.: Aerosol data assimilation using data from Himawari‐8, a next‐generation geostationary meteorological satellite, Geophysical Research Letters, 43, 5886-5894, 10.1002/2016gl069298, 2016.

Zhang, Y., Chen, J., Yang, H., Li, R., and Yu, Q.: Seasonal variation and potential source regions of PM2.5-bound PAHs in the megacity Beijing, China: Impact of regional transport, Environ Pollut, 231, 329-338, 10.1016/j.envpol.2017.08.025, 2017.

Zhu, S., Li, X., Yu, C., Wang, H., Wang, Y., and Miao, J.: Spatiotemporal Variations in Satellite-Based Formaldehyde (HCHO) in the Beijing-Tianjin-Hebei Region in China from 2005 to 2015, Atmosphere, 9, 10.3390/atmos9010005, 2018.